JOURNAL OF GEOPHYSICAL RESEARCH, VOL. 113, B03306, doi:10.1029/2005JB004193, 2008

Click Here for Full Article

Three-dimensional *S* velocity of the mantle in the Africa-Eurasia plate boundary region from phase arrival times and regional waveforms

C. Schmid,[1,2] S. van der Lee,[3] J. C. VanDecar,[4] E. R. Engdahl,[5] and D. Giardini[1]

Received 29 November 2005; revised 24 March 2007; accepted 6 July 2007; published 15 March 2008.

[1] A new model of the three-dimensional shear velocity structure of the Africa-Eurasia plate boundary is presented. The new model is derived by jointly inverting different types of seismic data. The two main sources of information are regional waveforms and teleseismic *S* wave arrival times. We show that it is possible to find a model that fit the different data types nearly as well as when inverting solely one type of data. The main improvement in resolving power is achieved between depths of 300 and 700 km, though the improvements are not limited to this depth range. Our model reflects the complicated evolution of this plate boundary area. The transition zone is dominated by high-velocity anomalies which we infer to represent a mix of lithosphere that subducted relatively recently or is not sufficiently cold and dense to traverse the 660-km discontinuity. The only low-velocity zone in the transition zone is beneath the Ionian Sea. The high-velocity Hellenic slab is continuous throughout the upper mantle and into the lower mantle to about 1200 km, most likely representing subducted Neo-Tethys lithosphere. The uppermost mantle is dominated by low velocities, consistent with the high level of tectonic activity. Low-velocity regions are relatively strong beneath the Mid-Atlantic Ridge, Turkey, and the Dead Sea region. The region's current lithosphere is relatively thin, except beneath the Adriatic and Ionian seas and the easternmost Atlantic Ocean.

Citation: Schmid, C., S. van der Lee, J. C. VanDecar, E. R. Engdahl, and D. Giardini (2008), Three-dimensional S velocity of the mantle in the Africa-Eurasia plate boundary region from phase arrival times and regional waveforms, *J. Geophys. Res.*, *113*, B03306, doi:10.1029/2005JB004193.

1. Introduction

[2] The plate boundary zone between Africa and Eurasia is characterized by many branches of high seismicity and deformation. The European mainland part of the of the plate boundary region is heavily instrumented with broadband seismic stations, capable of monitoring seismicity, tectonics, and deep structure. Broadband station coverage in Africa and the Azores is growing and temporary deployments of portable broadband stations have much enhanced this monitoring ability. Here we use a unique data set of broadband seismograms, augmented with teleseismic *S* wave arrival times, from the Eurasia-Africa plate boundary region to image the mantle beneath the plate boundary region. Our images are expected to be an improvement upon previous tomographic images for this region because of the enhanced data coverage and combination of different seismic data types with complementary resolving power.

1.1. Tectonic Background

[3] A topographic map (Figure 1) readily shows the large number of apparently scattered mountain belts and basins, and the spatially rapid transitions between them. The map is one piece of evidence of the complex tectonic history of the Mediterranean region. Large scale convergence cooperates with smaller zones of extension, and some strike-slip behavior. Below we briefly describe the key features of its evolution, for a more detailed overview the reader is referred to *Dercourt et al.* [1986], *Dewey et al.* [1989], and *Stampfli and Borel* [2004].

[4] Figure 1 also shows the main tectonic features. In the west, the plate boundary between Eurasia and Africa starts at the Azores triple junction. Eastward, it ends where the Eurasian plate meets the Anatolian plate and where the African plate borders the Arabian plate at the Dead Sea transform fault.

[5] The break up of Pangea in the Jurassic led to rifting and formation of new lithosphere (central Atlantic, Alpine-Tethys and other smaller oceans). The separation of Africa and Eurasia peaks in the Cretaceous (130 Ma) and after a translation phase, Africa-Eurasia convergence starts at around 85 Ma, although subduction of the new, Jurassic

[1]Institute of Geophysics, ETH Zurich, Zurich, Switzerland.
[2]Now at Schweizerische Mobiliar Versicherungsgesellschaft, Bern, Switzerland.
[3]Department of Earth and Planetary Sciences, Northwestern University, Evanston, Illinois, USA.
[4]Department of Terrestrial Magnetism, Carnegie Institute of Washington, Washington, D. C., USA.
[5]Department of Physics, University of Colorado, Boulder, Colorado, USA.

Copyright 2008 by the American Geophysical Union.
0148-0227/08/2005JB004193$09.00

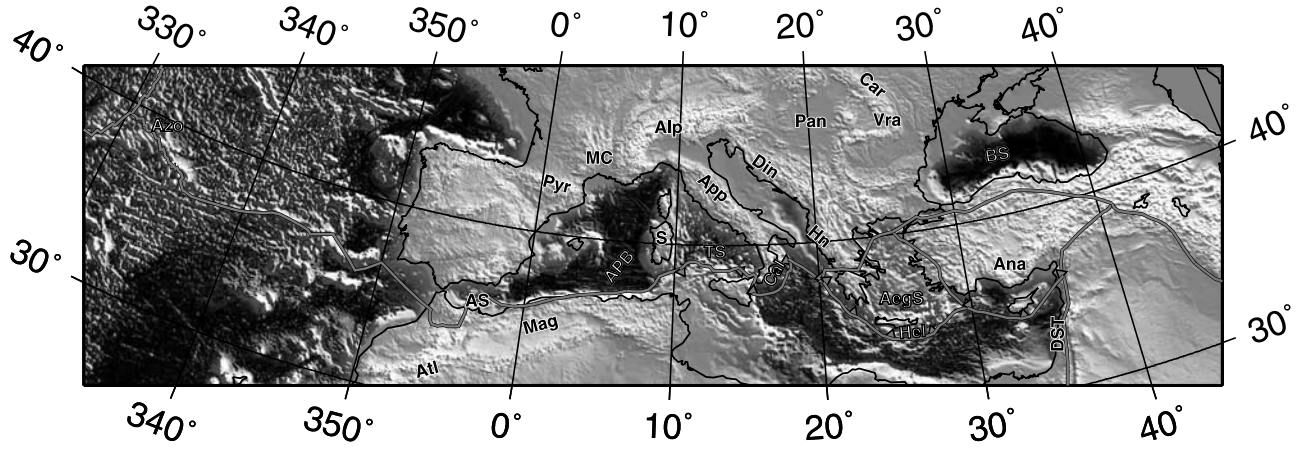

Figure 1. Topographic map and main tectonic features of the Mediterranean region. TS, Tyrrehenian Sea; Din, Dinarides; Cal, Calabrian Arc; Hel, Hellenic arc; App, Appenines; Mag, Maghrebides; AegS, Aegean Sea; DST, Dead Sea Transform; Pyr, Pyrenees; APB, Algero-Provençal Basin; Alp, Alps; Atl, Atlas; BS, Black Sea; Car, Carpathians; Azo, Azores; Pan, Pannonian Basin; AS, Alboran Sea; Vra, Vrancea; MC, Massif Central; S, Sardinia; Ana, Anatolia; Hn, Hellenides.

oceanic lithosphere had already been initiated during the extensional stages. This convergence between Africa and Eurasia has been the main stimulus for the last 85 m.y. The shortening was accompanied by oceanic lithosphere subducting into the mantle and mountain belts such as the Alps were formed.

[6] In the western Mediterranean, the northward directed subduction of the Ligurian Ocean (part of the Alpine-Tethys) beneath the east coast of Spain led to trench rollback, rapid extension, microplate rotation and drift and resulted in the formation of the Western Mediterranean Basins, the Alboran Sea, Liguro-Provencal basin and the Tyrrhenian Sea (Figure 1). At the same time extensional tectonics were also present further to the east, namely the Aegean Sea and the Pannonian basin. The common onset of extension in various smaller-scale domains around 30 Ma might be related to a slow down of absolute African plate motion [*Jolivet and Faccenna*, 2000]. At the surface, Mesozoic oceanic lithosphere has been preserved only in the Ionian Sea, which represents the last remnant of the once large Neo-Tethys ocean.

[7] Present-day active subduction has been imaged by seismic tomography for the Hellenic arc and the Calabrian arc [*Spakman et al.*, 1993]. In case of the Calabrian subduction zone, a well defined, albeit narrow, Wadati-Benioff zone is present down to about 500 km [*Selvaggi and Chiarabba*, 1995], a unique feature in the Mediterranean. The deepest (650 km) seismicity in the Mediterranean region is observed below southeastern Spain [*Buforn et al.*, 2004].

1.2. Three-Dimensional Structure of the Mantle

[8] The heterogeneous three-dimensional (3-D) structure of seismic velocity in the Mediterranean upper mantle characterizes causes and consequences of the complex tectonic history of the region. The velocity structure has been imaged with seismic tomography.

[9] Numerous models on various scales exist for the extended Mediterranean plate boundary region, which are based on the arrival times of *P* waves. Local models (using regional and/or teleseismic arrivals) cover small parts of the region (such as *Calvert et al.* [2000] or *Lippitsch et al.* [2003]). Regional *P* models include that from *Spakman et al.* [1993] or *Piromallo and Morelli* [2003]. The global *P* model of *Bijwaard et al.* [1998] also offers good resolution in the Mediterranean region owing to their use of regionally appropriate grid spacings.

[10] In contrast to these compressional velocity models, models of the shear velocity structure are mostly based on the inversion of data gained from analyses of surface waves. Phase or group velocity maps for example were obtained by *Panza et al.* [1980] or more recently *Pasyanos and Walter* [2002]. The model of *Marone et al.* [2004] (model EAV03) was derived using the partitioned waveform inversion (PWI) method [*Nolet*, 1990; *van der Lee and Nolet*, 1997], which uses surface waves in combination with regional *S* waves. Regional *S* models based on arrival times of body waves are shown by *Zielhuis* [1992] and *Bijwaard* [1999].

[11] This paper presents a new 3-D *S* velocity model for the Eurasia-Africa plate boundary region. We combine the regional waveform data set of *Marone et al.* [2004] with teleseismic body wave arrival times and external constraints on crustal thickness. From the joint usage of teleseismic arrival times and regional waveforms we derive better resolution because we simultaneously exploit their individual advantages. Teleseismic body wave arrival times and waveforms of regional *S* and surface waves have highly complementary resolving power. The body waves allow us (1) to image down to a depth of 1400 km, (2) to obtain excellent lateral resolution near stations arrays, and (3) to image small-scale features, while the regional *S* and surface waves allow us (1) to obtain good depth resolution, particularly in the uppermost mantle, (2) to image the upper mantle between station arrays and hypocenter populations, and (3) to constrain absolute rather than relative velocity variations. Variations on this approach have been successfully used on a more global scale [*Ritsema et al.*, 1999; *Dziewonski et al.*, 1975] and more local scale [*West et al.*, 2004]. We choose the Mediterranean region for application

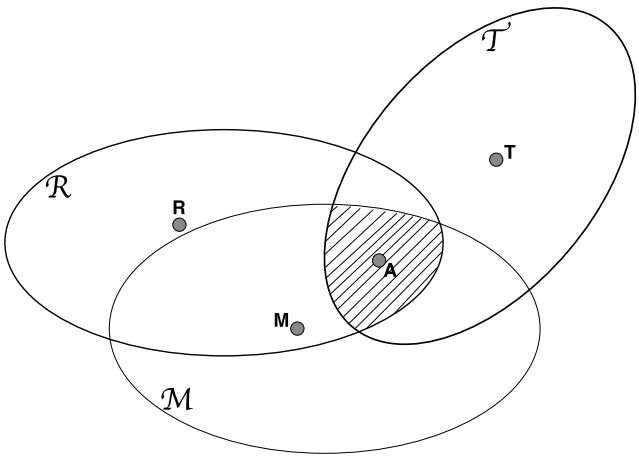

Figure 2. Venn diagram for the model space. $\mathcal{R}$, $\mathcal{T}$, and $\mathcal{M}$, are the sets for all possible models that predict acceptable fits to the regional waveforms, the traveltimes, or the Moho constraints, respectively. **R**, **T**, and **M**, are typical examples of preferred models that might result from inverting any of these data sets alone. Typically, such models do not naturally fit all other data sets. In a joint inversion, we only search for acceptable models in the hatched region, which represents the intersection of the three sets, $\mathcal{R} \cap \mathcal{T} \cap \mathcal{M}$. The hatched region contains all possible models that predict acceptable fits to each of the three data sets. Model **A** in the hatched region is a typical result of a joint inversion, such as that presented in this paper.

of our new joint inversion because it has been well studied. Our approach unifies some structural features in the Mediterranean mantle from different models into one model, simultaneously narrowing the range of possible models for this region (Figure 2). This approach better constrains these structures and shows only their characteristics that are consistent with both data sets. We then proceed to interpret our model in the context of recent literature on the tectonic history of the region.

2. Method

[12] Both body wave traveltimes and regional waveform fits are generally cast as linear constraints on seismic velocity (or slowness) of the Earth's interior. We combine these constraints into a single set of linear equations, which we aim to solve for the velocity structure of the mantle beneath the Mediterranean region.

[13] For regional waveform fitting, we use the method of partitioned waveform inversion (PWI) [*Nolet*, 1990]. The first part of PWI is a nonlinear waveform fitting procedure, where one finds for a number of recordings the 1-D models that best fit the observed waveforms with synthetic seismograms. In the second step the linear constraints on path-averaged velocity structure yielded by the waveform fitting are combined from many seismogram fits and solved for a 3-D velocity model. This second step can be written as

$$(\mathbf{A^{sw}})m = d^{sw} \tag{1}$$

where $\mathbf{A^{sw}}$ relates the model vector m to a data vector d^{sw}. Details on equation (1) are given by *Nolet* [1990] and *van der Lee and Nolet* [1997]. Model m contains perturbations of the 3-D velocity field, Δv, as well as perturbations in Moho depth, Δh. The role of Moho depth in modeling waveforms was incorporated into the PWI by *Das and Nolet* [1995].

[14] The traveltime equation has second-order terms equal to zero according to Fermat's principle. Ignoring third- and higher-order terms, the traveltime equation is given by

$$\delta t \approx -\int_{L_0} \frac{1}{v_0}\frac{\delta v}{v_0} \mathrm{d}l \tag{2}$$

where δt is the time delay accumulated along the unperturbed raypath L_0 with velocity perturbations δv. v_0 is the velocity of the background model. In discrete form equation (2) for the ith observation can be written as

$$\Delta t_i = A^{bw}_{ij_v}\Delta v_{j_v} + \Delta x^{e_i}\nabla E_i + \Delta e_i + A^{bw}_{ij_m}\Delta h_{j_m} \tag{3}$$

where matrix elements A^{bw}_{ijv} contain the numerically determined partial derivatives with respect to velocity of the ith delay time $\Delta\ t_i$ to the velocity v_{jv} of the j_vth model node and A^{bw}_{ijm} contain the delay time derivatives to the Moho perturbation Δh_{jm} of the j_mth node The velocity and Moho depth of the model are consecutive elements of the model vector where $1 \le j_v \le N_v$ and $N_v + 1 \le j_m \le N_v + N_m$, and N_v and N_m are the number of velocity nodes and Moho nodes in the model, respectively. Because a teleseismic ray rarely goes exactly through a Moho model node, up to three Moho model nodes (the corners of the triangle in which the ray intersects the Moho) are affected by the ray. Rays are traced according to *VanDecar* [1991]. ∇E_i are the partial derivatives of the arrival times to the hypocentral location. We also added the correction vector Δx^e_i for the hypocenter that produced the ith delay time and the origin time correction term Δe_i for the same earthquake. In pure teleseismic traveltime inversions, one does not solve for Moho perturbations due the large trade off with the station term and the velocity heterogeneity. The combination of traveltimes with regional waveforms, however, make Moho depth a resolvable model parameter.

[15] Equation (3) also is a linear system of equations and can be combined with equations (1), so that we obtain the coupled system

$$\mathbf{A}m = d \tag{4}$$

or written out,

$$\begin{bmatrix} \mathbf{A^{bw}} & \mathbf{A^{bw}_m} & \nabla E \\ \mathbf{A^{sw}} & \mathbf{A^{sw}_m} & 0 \\ 0 & \mathbf{A^{rf}_m} & 0 \end{bmatrix} \begin{bmatrix} \Delta v \\ \Delta h \\ \Delta x_e \end{bmatrix} = \begin{bmatrix} d^{bw} \\ d^{sw} \\ d^{rf} \end{bmatrix} \tag{5}$$

[16] Matrix $\mathbf{A}$ and $\mathbf{A_m}$ contain the partial derivatives of the data to velocity and Moho depth perturbations, respectively, and $d^{bw} = \Delta t$. The matrix $\mathbf{A^{rf}_m}$ and data vector d^{rf} represent point constraints on Moho depth, incorporated

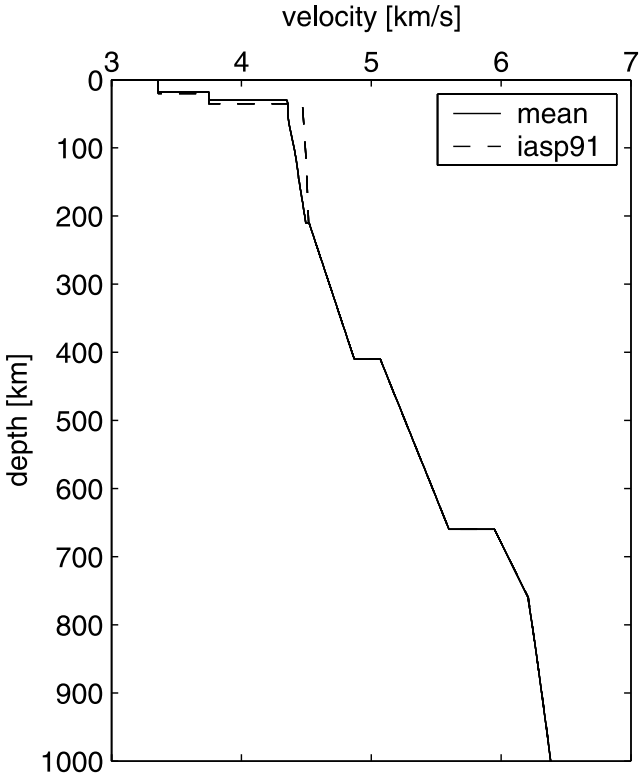

Figure 3. One-dimensional reference models. MEAN is the reference model used in this paper. It is identical to the model used in EAV03 and identical to iasp91 below 210 km.

into the inversion as in the work by *Das and Nolet* [1998], *van der Lee et al.* [2001a], and *Marone et al.* [2003]. These point constraints are extracted from published results from active source experiments, such as refraction lines, and receiver function studies in our study region [*Marone et al.*, 2003]. In these constraints $\mathbf{A_m^{rf}}$ is derived from the location of the study and $\mathbf{d^{rf}}$ represents the results of the study for Moho depth at that location. We scale the equations by the reciprocal of the measurement error through a diagonal data covariance matrix. We assume that the off-diagonal elements of the data covariance matrix $\mathbf{C_d}$ are zero, which is largely valid for the arrival times because we invert for systematic factors such as earthquake mislocations, and for the regional waveforms because we diagonalize the Hessian matrix of the misfit function before defining the linear equations in equation (1) [*Nolet*, 1990].

[17] We do not include the station term in equation (5) because they represent shallow crustal structure, which is included in estimates of average crustal velocities constrained by the regional waveforms. Data from waveforms of regional body and surface waves complement traveltime data of teleseismic body waves because the former waves travel predominantly horizontally while the latter waves travel predominantly vertically.

[18] The problem in equation (5) is simultaneously overdetermined and underdetermined, because of the nonuniform coverage of the model by the data. Because of the underdetermined part, we need to add additional a priori constraints on the solution. We apply norm damping and first derivative damping [*Constable et al.*, 1987; *VanDecar*, 1991], so that the regularization operator is given by

$$\mathbf{R} = \begin{bmatrix} \alpha\mathbf{I} \\ \lambda_h\mathbf{F_h} \\ \lambda_v\mathbf{F_v} \end{bmatrix} \tag{6}$$

where $\mathbf{I}$ is the identity matrix, $\mathbf{F_h}$ and $\mathbf{F_v}$ are the flattening operator in the horizontal and vertical directions, respectively, and α and λ are weights. Note that we use different weights in the horizontal and vertical direction. A similar operator is used for the Moho perturbations, obviously without vertical flattening.

[19] We solve equation (4) using conjugate gradients [*Scales*, 1987; *VanDecar*, 1991].

3. Model Parameterization

[20] We define seismic velocity and Moho depth through trilinear and bilinear, respectively, interpolation between nodes n a grid. The grid consists of spherical shells at various depths, with internode distance increasing with depth from 50 km in the uppermost mantle to 200 km in the lower mantle. The grid points within each shell are derived through triangular tessellation as described by *Wang and Dahlen* [1995] and used by *van der Lee and Nolet* [1997] for parameterizing Moho depth. The horizontal grid spacing is approximately 75 km. The center of the grid is at 34°N/14°E and extents from here approximately 40° in all directions. In depth, the grid reaches down to the core-mantle boundary. This results in about 340000 (10636·32) nodes containing unknown velocity perturbations. An additional number of unknowns arises from the Moho perturbations. These were discretized on the same lateral grid, so that the number of unknowns amounts in total to 350000. However, only about 60% of these are sensed by our data, yielding 207015 the effective number of unknowns. The spatial extent of the grid outreaches the parts where we expect to achieve good resolution. By choosing such a large grid we try to minimize the mapping of external structure into the regions of interest.

[21] We use a 1-D background model called "MEAN" (Figure 3), which is iasp91 [*Kennett and Engdahl*, 1991] modified to thinner crust and lower velocities in the uppermost mantle to reflect regionally averaged structure for the Eurasia-Africa plate boundary region [*Marone et al.*, 2003]. The model was used as background model for 3-D model EAV03 [*Marone et al.*, 2004].

4. Data

[22] We used seismograms from earthquakes worldwide and stations in the Eurasia-Africa plate boundary region. Permanent stations are from MedNet [*Boschi et al.*, 1991], Geofon [*Hanka and Kind*, 1994], Geoscope [*Romanowicz et al.*, 1984], and national agencies (Swiss National Network [*Baer*, 1990], Universita di Trieste, RéNaSS, TGRS, GRSN, GRF, Universität Stuttgart, GII, Universitat de Barcelona, Universidad Autónoma de Madrid, Institute Andaluz, Czech National Seismological Network, NARS, GI_Budapest and Blacknest).

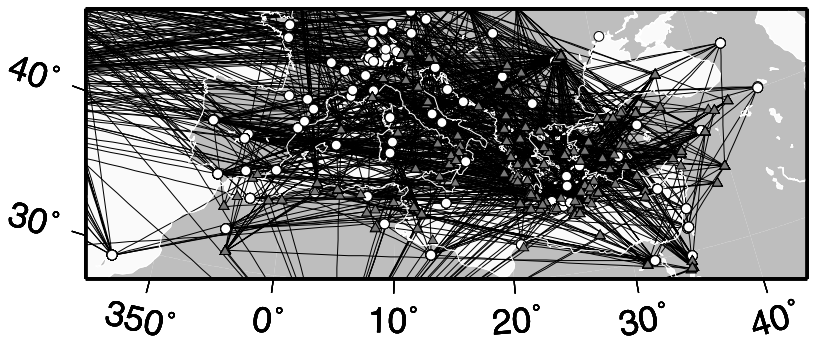

Figure 4. Map of surface wave raypaths. Circles give location of stations, and the triangles show the earthquake location.

[23] Additional seismogram data were collected from temporary broadband seismic experiments, including Geofon and in particular MIDSEA [*van der Lee et al.*, 2001b]. MIDSEA was designed to improve imaging resolution in the Eurasia-Africa plate boundary region and consequently includes broadband stations from Mediterranean islands, northern Africa, and the Azores. This wealth of new data from unique locations combined with our novel joint tomographic approach yields a significantly sharper tomographic *S* velocity model for the region than heretofore possible.

4.1. Surface Wave Data

[24] We used the regional waveform data from *Marone et al.* [2004]. This data set consists of waveform fits for the fundamental and higher mode surface waves for 1136 seismograms, resulting in a total of 8714 surface wave constraints. Figure 4 shows the surface wave raypath coverage along with the stations where seismograms were recorded. The median path length is around 15° [*Marone et al.*, 2003] and body waves with paths that bottom in the lower mantle were not used to avoid the regime where 1-D sensitivity kernels are no longer a fair approximation to the laterally varying sensitivity of body waves.

4.2. Body Wave Data

[25] We use arrival time data from two different sources. We correct both traveltime data sets for topography before inversion.

[26] First we use relative arrival times of teleseismic *S* waves (distance range 30°–90°) that were measured in broadband seismograms [*Schmid et al.*, 2004] using the multi channel cross correlation method [*VanDecar and Crosson*, 1990]. These broadband seismograms are from the temporary MIDSEA array [*van der Lee et al.*, 2001b] and the permanent Geofon [*Hanka and Kind*, 1994] and MedNet [*Boschi et al.*, 1991] networks. A station map is shown in Figure 5. The delays were measured on the transverse component. This analysis produced 3000+ high-quality relative *S* arrivals in total. Even though the formal error, as determined by the cross correlation, can be as low as a tenth of a second, we use an uncertainty of at least 0.3 s when weighting the data during inversion.

[27] A second data set consists of the reprocessed [*Engdahl et al.*, 1998; E. R. Engdahl, personal communication, 2004] *S* arrival time data of the ISC for the years 1964–2002. From this global data set we extracted *S* arrival times at stations in the larger Mediterranean region (Figure 5) that have a reported arrival time precision of 1 s or less. We used an upper distance limit of 80° in order to omit difficulties with the *SKS* phase crossing at ~83°. The lower limit is at 20°. This set provides around 30000 arrival times, which is significantly more than those we measured interactively by cross correlation. However, this ISC data set is inferior in quality, since the arrivals were picked on onset, which is often emergent, by multiple operators on individual seismograms, and thus also lacking consistent error esti-

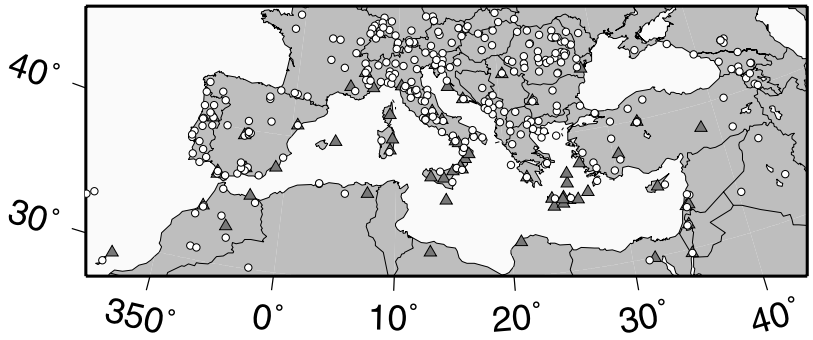

Figure 5. Map of stations used with body arrival time data. Circles give stations for which we extracted absolute delays from the reprocessed [*Engdahl et al.*, 1998] catalog of the International Seismological Centre (ISC), and the triangles represent stations with high-quality relative delays obtained using cross correlation.

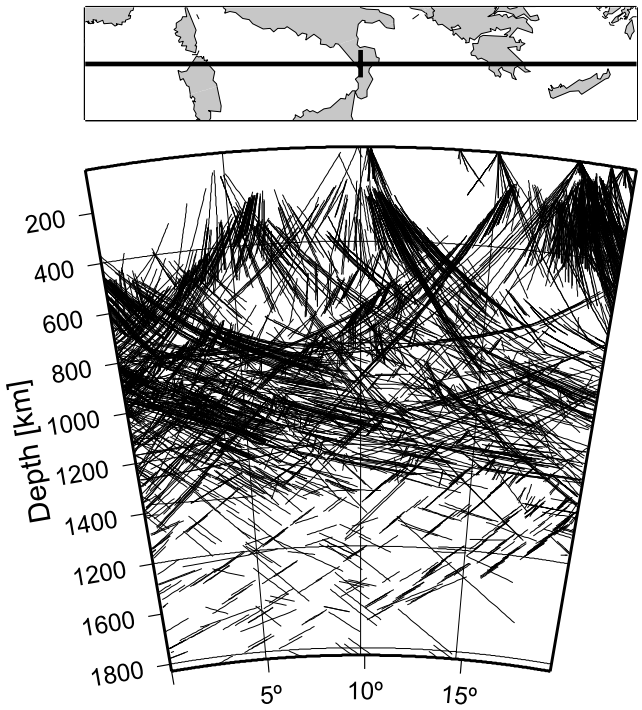

Figure 6. Body wave raypaths. Raypaths inside 1° from the vertical profile plane were projected onto that plane. Note the absence of raypaths in the upper mantle beneath the seas.

mates. *Röhm et al.* [2000] identified many outliers and systematic errors in this data set. Therefore we presume each arrival time to have an uncertainty of 1.0 s or more.

[28] Although the amount of combined body wave traveltime data is relatively large, their wave path coverage is not ideal. First, even though the MIDSEA stations prove to be a very valuable addition for the southern part of the Mediterranean region, the station coverage here remained sparser than on the European mainland to the north. Secondly, the obvious presence of the Mediterranean sea made a homogenous station coverage impossible. Therefore in the upper 300 km, there is a relative lack of crossing body wave paths or even no paths at all in some places, as illustrated by Figure 6. Figure 6 further shows that the best crossing raypath coverage for this region occurs roughly between 700 and 1300 km in depth. Consequently, we expect the best body wave resolving power at these depths, which perfectly complements the resolving power for the upper mantle provided by the regional waveform fits of *Marone et al.* [2004].

4.3. Moho Constraints

[29] To additionally constrain the crustal thickness we use data from three different sources: receiver function studies, seismic refraction profiles and gravity studies. These data give information on crustal thickness at specific points. We use different uncertainties depending on the type of data. Full details of these data, including references, are given by *Marone et al.* [2003]. In this study we additionally use data from the receiver function study of *Diehl* [2003].

5. Resolution Analysis

[30] Because of the large size and the underdetermined part of our inversion problem, a quantitative estimate of the error in the tomographic model is not feasible. To give some estimate of the reliability of the final model, we rely on resolution tests. We calculate a synthetic data vector $\mathbf{d}_s$ by multiplying matrix $\mathbf{A}$ of equation (4) with a synthetic model vector $\mathbf{m}_s$. After the addition of noise, we invert $\mathbf{d}_s$ to obtain a recovered model $\mathbf{m}_r$, which would be identical to $\mathbf{m}_s$ in the ideal case.

[31] Figure 7 shows the outcome for a synthetic model with a harmonic input structure. Figure 7 illustrates resolving power for the teleseismic traveltimes and regional waveforms separately as well as combined. Results of tests with realistic geodynamic features are shown in section 6. It is evident (Figure 7) that the regional waveforms have excellent sensitivity to uppermost mantle, but with increasing depth, the resolving power decreases. The opposite is true for the arrival time data. Recovered shallow anomalies are either smeared in the radial direction owing to the vertical incidence or completely absent when there are no stations at the surface such as is the case beneath the sparsely covered African coast or the Mediterranean Sea. However, starting at around 300 km, the input features become well resolved and only when going deeper than about 1300 km the resolution decreases and anomalies smear. The gain in using a joint inversion is not only that structure is continuously well recovered from the shallow parts down to 1300 km, but we also achieve better resolution for the parts that more than one of the data sets are sensitive to, such as the transition zone. The lower mantle is better resolved in the joint inversion than with teleseismic arrival times alone because the regional waveforms help the arrival times to separate the effects of upper mantle structure from those of lower mantle structure.

6. Results

[32] An important assumption we made in section 5 is that body wave delay times and regional waveform misfits are caused by the same 3-D structure rather than different structures in different locations or at different scales. This assumption may not be entirely valid because of the difference in frequency content and associated Fresnel zone size between the data sets. High-frequency traveltimes (such as many in the ISC catalogue) might be most sensitive to small-scale structure while longer-period regional waveforms would be sensitive to larger-scale structures. Nevertheless, ISC traveltime inversions show fairly smooth, continuous large-scale structures, such as subducting slabs [*Spakman et al.*, 1993; *van der Lee*, 1990], of similar size as structures sensed and imaged by regional waveforms [*Zielhuis and Nolet*, 1994]. If these large-scale structures imaged by high-frequency traveltimes are the result of spatial aliasing, the arrival times should strongly depend on frequency. However, *Schmid et al.* [2004] demonstrated that the frequency dependence of body wave delay times

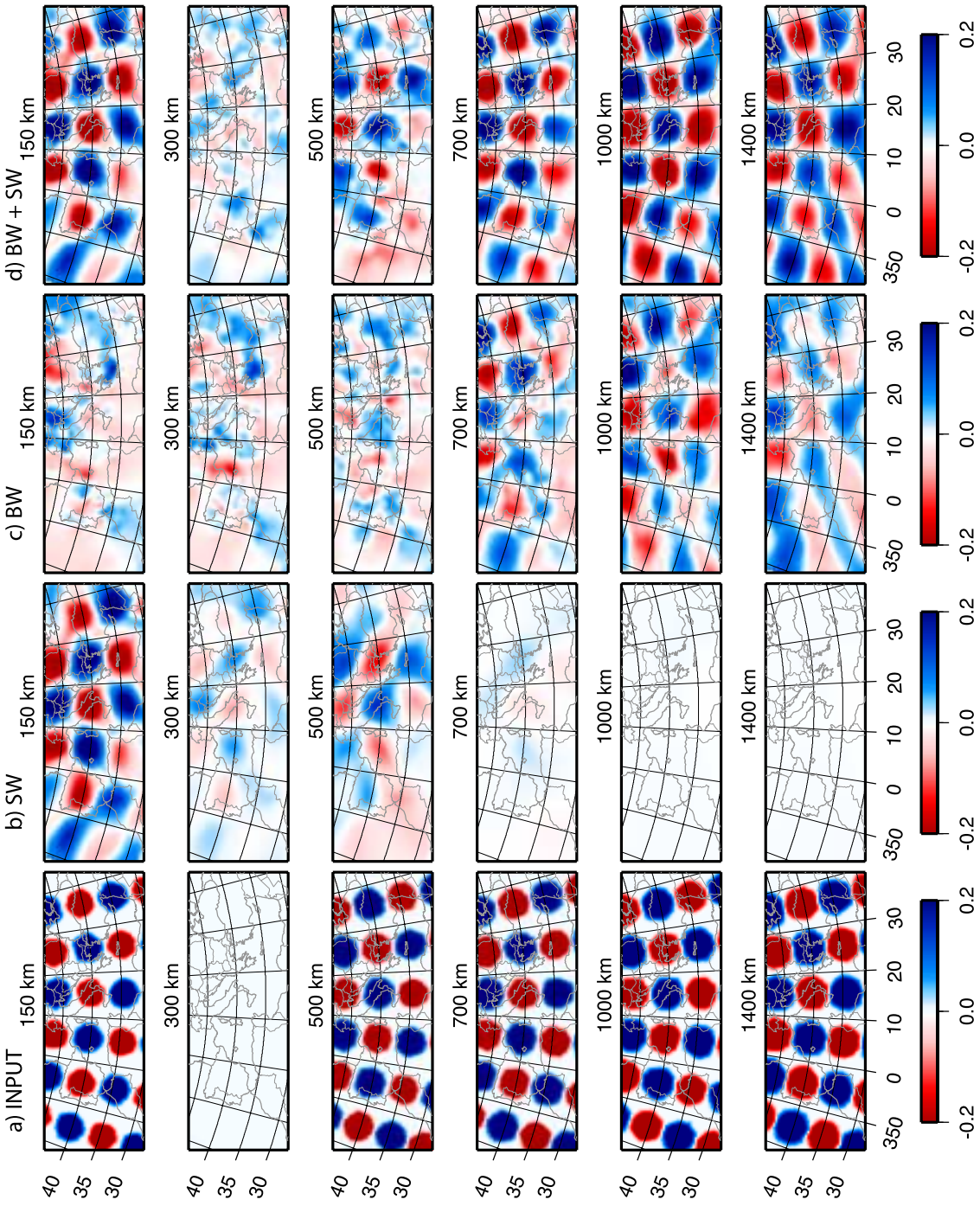

Figure 7. Results of a harmonic test for depths of 100, 300, 500, 700, 1000, and 1400 km. (a) Input model, (b) regional waveforms, (c) *S* arrival times, and (d) joint inversion.

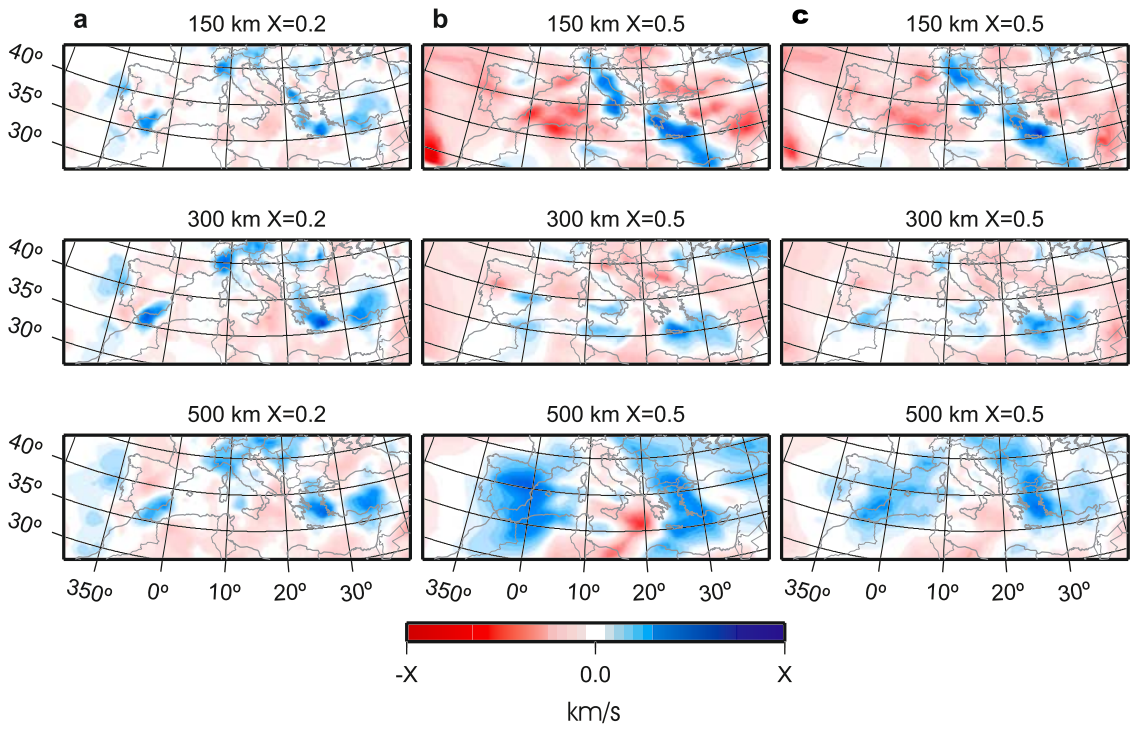

Figure 8. Horizontal slices at upper mantle depths (150, 300 and 500 km) of the preferred models based (a) solely on *S* arrival times, (b) solely on regional waveforms, or (c) on both data sets.

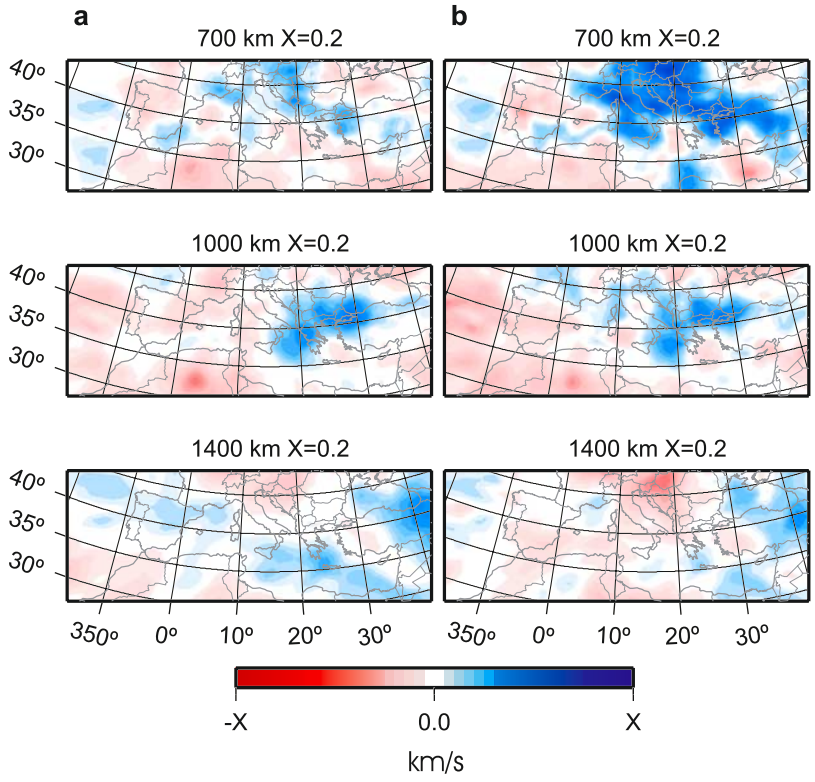

Figure 9. Horizontal slices at lower mantle depths (700, 1000 and 1400 km) of the preferred models. (a) *S* arrival times and (b) joint inversion.

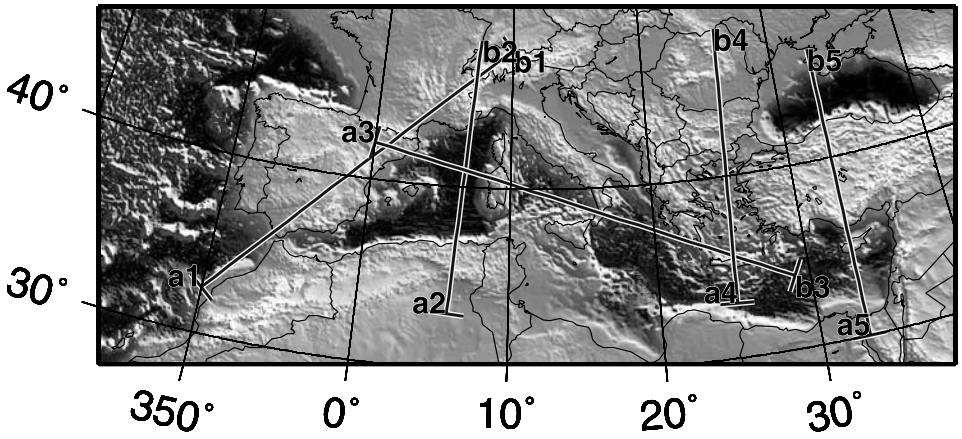

Figure 10. Map indicating the location of the cross sections shown in Figures 11–15.

only partly follows the systematic expected from structural anomalies smaller than a couple of hundred km and that part is small. This is encouraging in that it suggests that teleseismic delay times and regional waveforms may indeed be largely explained by the same 3-D structure. Our joint inversion further tests this hypothesis by investigating whether one 3-D model can simultaneously explain both data sets equally well as different models would explain the different data sets independently. First we explore the structural implications of each data set separately, then jointly. This will be followed by a discussion of the features of 3-D *S* velocity model obtained in the joint inversion and the most important differences to the single data models. Maps for the individual models are shown in Figures 8 and 9. The regional waveform data does not include waves with turning points in the lower mantle and thus they have no sensitivity to lower mantle structure. However, because the regional waveforms constrain the upper mantle structure well, upper and lower mantle structure can be better separated (and resolved) in an inversion that includes the waveforms as well as teleseismic delay times, which are sensitive to both. Figure 10 gives an overview map for the locations of all cross sections shown in Figures 11–15.

[33] The fast anomalies seen throughout the Mediterranean boundary region are most straightforwardly interpreted as temperature anomalies caused by subducted relatively cold oceanic lithosphere. The observed ratio of delay time of teleseismic *S* and *P* waves also suggests a predominantly thermal origin for the delays [*Schmid et al.*, 2004] and thus for the anomalies imaged from their inversion.

6.1. Regional Waveform Inversions

[34] We inverted the same constraints on mantle structure that *Marone et al.* [2004] used to construct 3-D *S* velocity model EAV03. They derived these constraints from fitting the *S* and surface waveforms of regional seismograms. This model has been analyzed extensively and the parameters regularizing the inversion have been chosen to balance data fit and model smoothness. However, our version of EAV03 (Figure 8b) looks slightly different from EAV03 [*Marone et al.*, 2004] because of differences in spatial parameterization and in the implementation of regularization (see section 2). Our model achieves the same variance reduction of 96% as of EAV03 of *Marone et al.* [2004].

[35] However, this model,derived from regional waveforms alone, does not explain the teleseismic delay times well and analogously, a model derived from teleseismic arrival times alone does not fit the regional waveform data well. Because each of these tomographic inversions is partly underdetermined there must exist other models that explain the data equally well. A joint inversion leads us to such a model, which simultaneously fits each data set virtually as well as the aforementioned models.

[36] Figure 8b shows that the regional waveforms sensed cold high-velocity material around 100 km depth, related to subduction of the Adriatic Plate beneath Italy and of the African Plate beneath the Aegean Sea and adjacent Greece and Turkey. Cold high-velocity material is wide spread in the transition zone (500 km), related to fragments of subducted lithosphere subducted in the relatively recent geologic past [*Marone et al.*, 2004]. The regional waveforms further reveal the extensive presence of weak low-velocity material, preferentially beneath the seas and ocean but also beneath plateaus and sedimentary basins. A prominent, isolated, vertically coherent low-velocity anomaly is imaged in the deeper upper mantle beneath the Ionian Sea, east of Sicily.

6.2. Body Wave Arrival Time Inversions

[37] Figures 8a and 9a show maps through our preferred body wave model. We experimented with various amounts of damping and flattening, the preferred model gives the best trade-off between data fit and model roughness. The variance reduction obtained is 97% for the high-quality lower-quantity cross-correlated delay times and 70% for the lower-quality large-quantity reprocessed ISC data set. In both cases, the root mean square residual is still larger than the measurement uncertainty. We also inverted for models based only on one of the two body wave data sets and obtained only slightly larger variance reductions with similar models for the parts were resolution is good. This shows that these data sets are fully compatible and enhances our confidence in the imaged structure.

[38] The lower variance reduction obtained with the ISC data is a result of the lesser quality of the ISC data. Therefore we choose to use a robust inversion technique of iterative residual downweighting [*Huber*, 1981; *VanDecar*, 1991] for the ISC part of the data. After 2000 iterations of the conjugate gradient equation solver, we weight down outliers

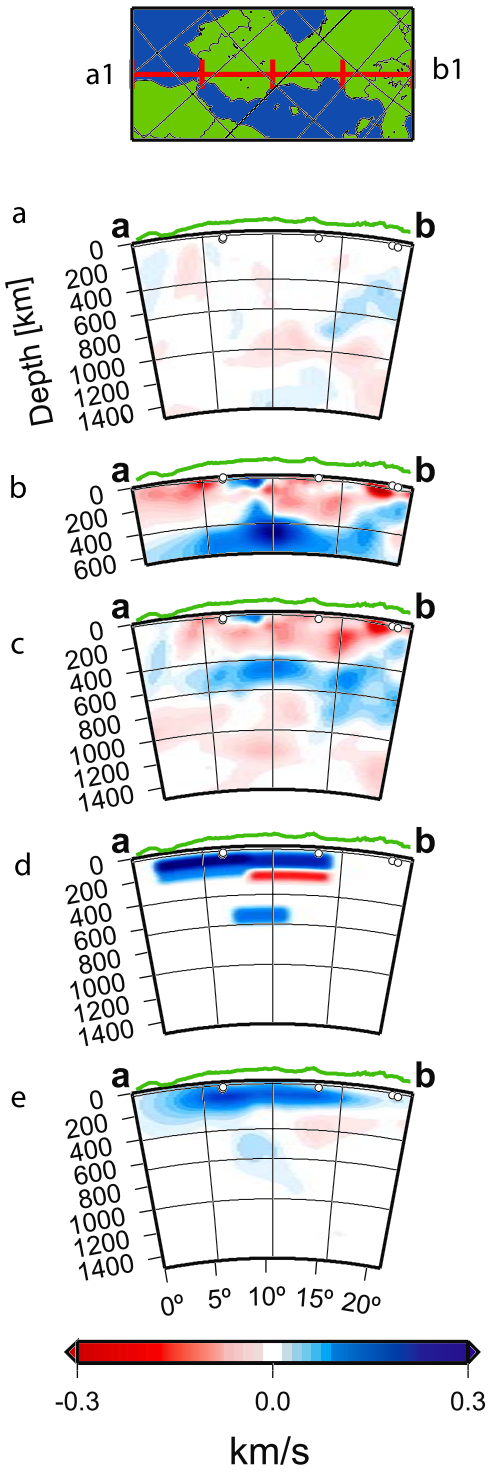

Figure 11. Cross sections through the preferred models for section a1–b1 using (a) only phase arrival time, (b) only the regional waveform data, (c) using both in a joint inversion, (d) input for a joint resolution test, and (e) output of the joint resolution test.

that are larger than 1.5 standard deviations. This step is repeated 10 times. The factor by which we downweight is chosen in a way that it has the effect of applying the L_1 norm to calculate the total misfit. The variance reduction stated above is the one achieved after the first 2000 iterations, before any downweighting is done. At that stage the variance reduction of the cross correlated part of the data is already close to the final one.

[39] The model resulting from the body wave arrival time inversion (Figures 8a and 9a) has not been previously published. We discuss it briefly here, before moving on to the model from the joint inversion. Down to about 300 km, several relatively fast anomalies have been imaged beneath

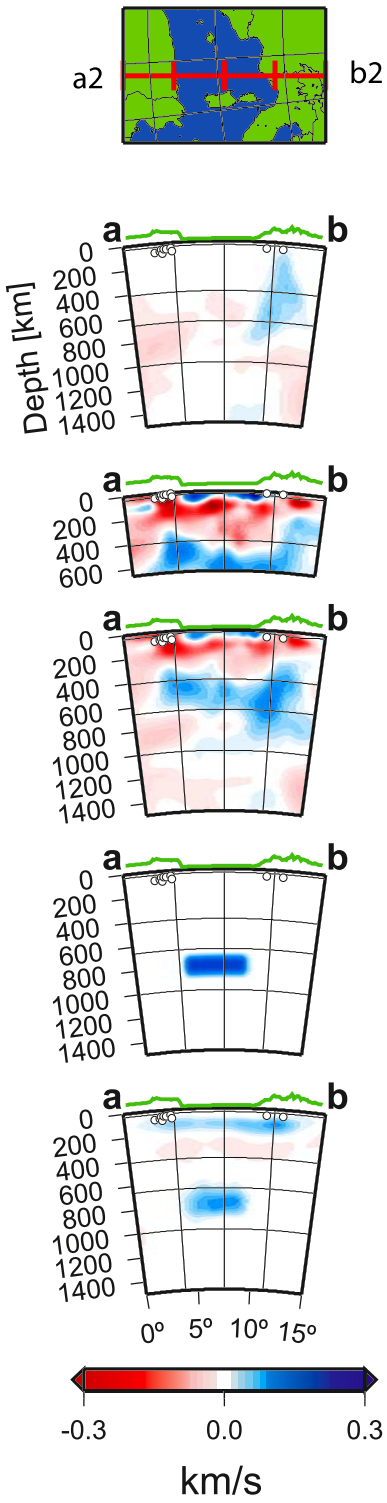

Figure 12. Same as Figure 11 for section a5–b5.

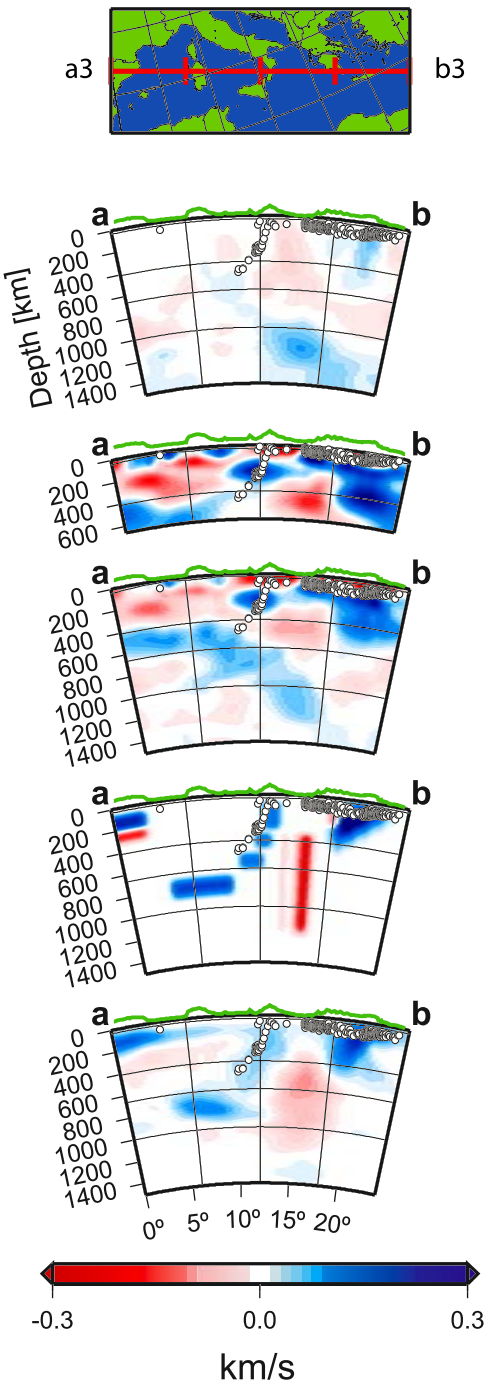

Figure 13. Same as Figure 11 for section a3–b3.

southern Spain, northwestern Italy, the Aegean Sea and north of Cyprus. These anomalies again relate to subducting or subducted lithosphere. The anomalies continue into the transition zone (500 km) where they become stronger and/or more extensive. Penetration of subducting lithosphere into the lower mantle (1000 km) is imaged only north of the Aegean Sea and Turkey, confirming the earliest tomographic images of this phenomenon [*Spakman et al.*, 1993]. These high-velocity anomalies are interpreted as relatively cold subducted lithosphere from the Alpine Tethys and Neotethys oceans, the latter still attached to surface lithosphere of the Ionian Sea and Levantine Basin, subducting beneath the Calabria and Hellenic arcs, respectively. However, the high-velocity anomaly at 1000–1200 km beneath the Ionian Sea is rather unrelated to Alpine- or Neotethyan subduction. This lower mantle anomaly also appears in the majority of global *P* velocity models but has not yet been identified. Assuming that the lower mantle is not as effective in staying with tectonic plates moving across the surface, the anomaly could result from subduction of the

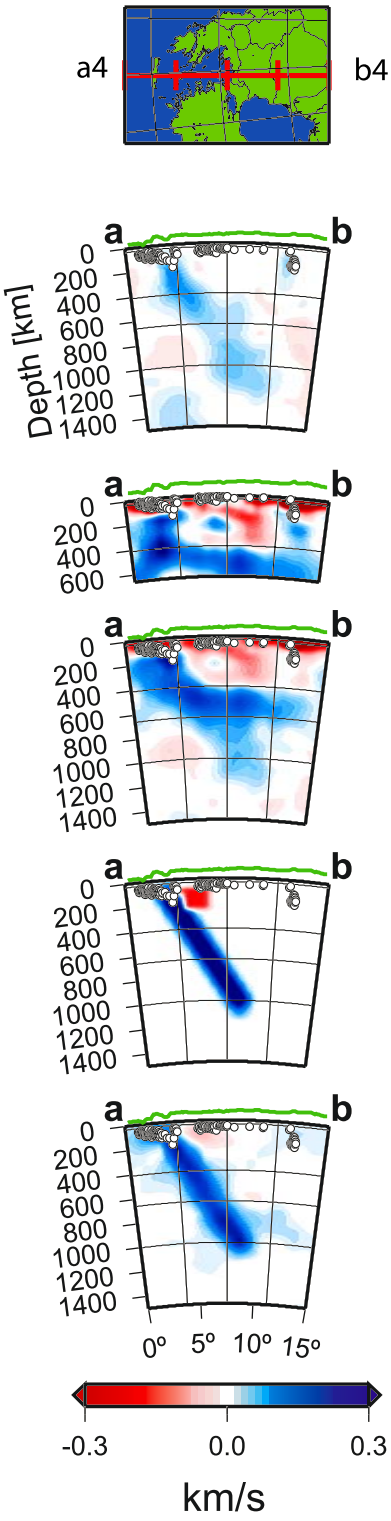

Figure 14. Same as Figure 11 for section a4–b4.

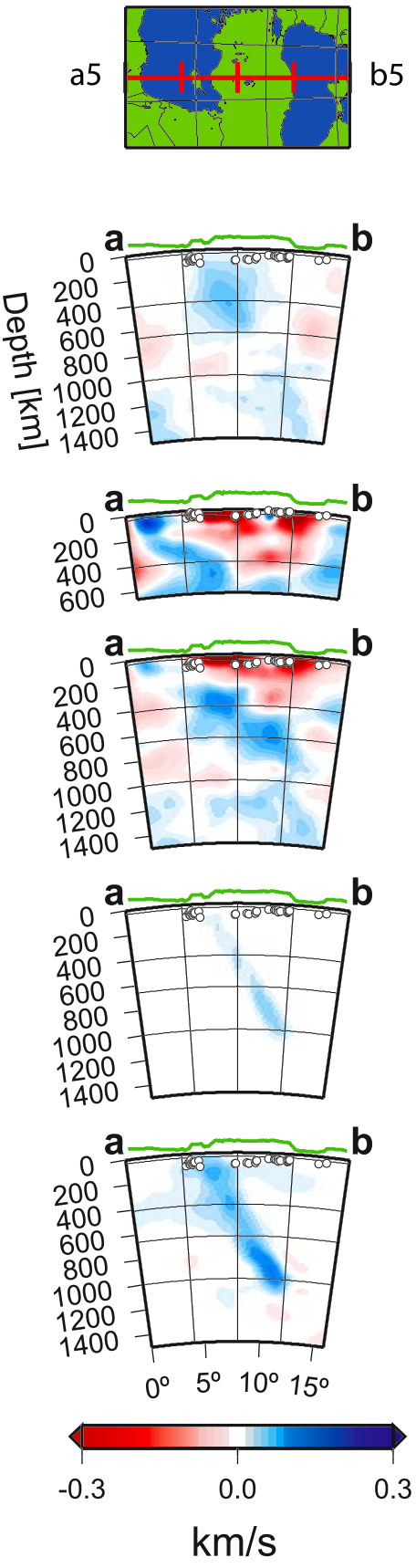

Figure 15. Same as Figure 11 for section a5–b5.

Vardar Ocean in the late Cretaceous or the westernmost area of the Paleothethys Ocean in the Triassic, when Europe and Africa were located much further south from the present latitudes [*Stampfli and Borel*, 2004]. The 2nd explanation is less likely than the first, Vardar subduction, because of thermal diffusion having had much less time to equilibrate Vardar lithospheric temperatures than Paleothethys lithospheric temperatures.

6.3. Comparison Between the Two Single Data Set Models

[40] The major difference between the two models obtained from inverting a single data set is that the arrival time model has much smaller anomaly amplitudes than the regional waveform model. This amplitude difference is mostly a result of teleseismic arrival times being insensitive to the strong vertical variations in the uppermost mantle sensed by the regional waveforms. The regional waveforms image a rather layered structure with a high-velocity lithosphere over a very low velocity asthenosphere. At these depths teleseismic raypaths are nearly vertical and essentially record the sum of the layers's effects on the traveltime, which is much smaller than the effect of each individual layer, yielding the rays practically insensitive to these vertical variations.

[41] Additional factors that cause differences in tomographic images between the two data sets are differences in the sensitivity kernels and in wave path coverage. The sensitivity of high-frequency teleseismic body waves stretches to the short-wavelength part of the structure spectrum, while that of longer-period regional waveforms stretches to the long-wavelength part of the spectrum. Differences in wave path coverage of the mantle volume are obvious for the lower mantle as seen by the waveform data or beneath the shallow Atlantic in case of the phase arrival data. In either case, the volumes are not sampled by the data and thus nothing can be imaged there by the single data set. Further differences occur where the mantle is sampled only in one spatial direction, causing strong smearing (see Figure 7).

[42] The two models also have features in common. For example, the high-velocity anomaly related to relatively cold African lithosphere subducting beneath the Hellenic arc (Figure 14) has been imaged down to the lower mantle by both data sets independently. For another example, both data sets image the high velocities of the subducted northern part of lithosphere of the Alpine Tethys (Figures 11 and 12). As a last example, both the teleseismic arrival times and the regional waveforms infer an important deep low-velocity anomaly beneath the Ionian Sea (Figure 13), which is somewhat smeared vertically by the arrival times and confined to the transition zone by the regional waveforms.

6.4. Joint Model Inversions

[43] We tried different amounts of weighting each data set in order to find the best fit to both data sets. Figure 16 shows the trade-off curve for fitting both sets of data while keeping model roughness on the same level. For Figure 16 we did not solve for station and earthquake terms, so that variance reduction is achieved completely via velocity perturbations. Weighting one set much stronger than the other set results in a poor fit for the latter. Decreasing the

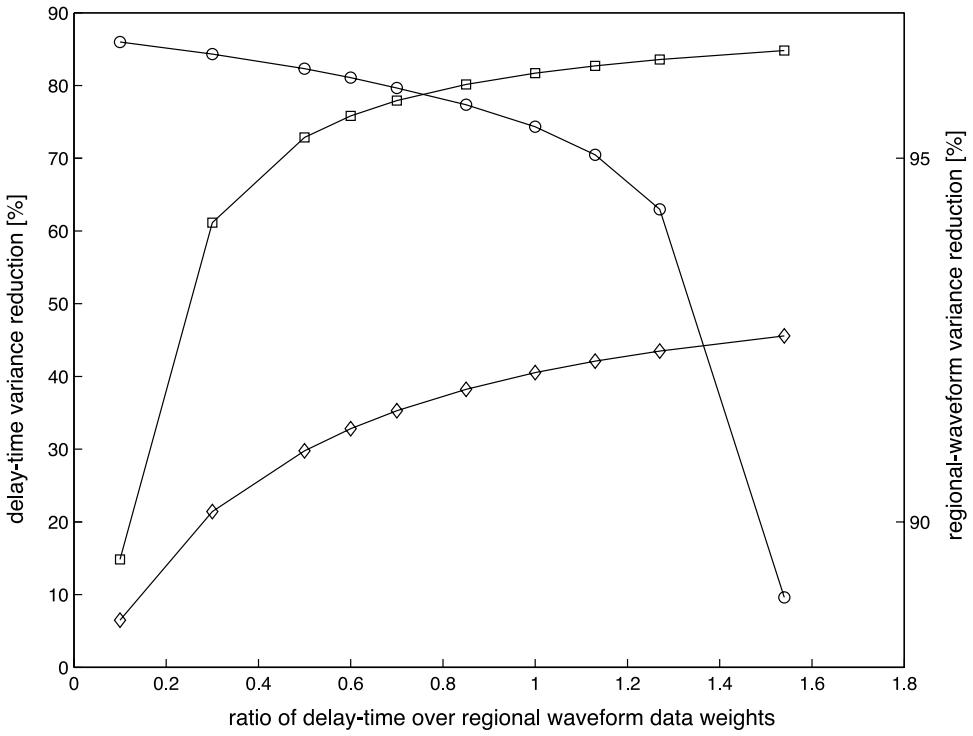

Figure 16. Variance reduction as a function of the relative scaling between phase arrival time data and the waveform data. Circles are for the waveform data, and the squares and diamonds denote the two phase arrival sets.

weight of the first set while increasing the second set, results in only a slightly poorer fit for the first one while the fit to the second set is strongly improved. Repeating this step several times we will eventually reach the situation where the fit to first set will be significantly decreased while only a slight improvement can be gained for the second set. We can achieve satisfactory fits to both data sets if the teleseismic delay time data are weighted 0.6 to 0.9 times the weight for the regional waveform data. The preferred model was then obtained by optimizing the trade-off between solution norm and model norm/roughness while employing a weight ratio of 0.8, which means that we weight the regional waveforms slightly more than the teleseismic delay times. The delay times, however, intrinsically weigh in heavily because of their larger number. The variance reduction for each of the data sets is about 1% lower than in the single data set inversions. Thus we have found an alternate model which is superior to the single data set models because it can simultaneously fit two different data sets at the expense of only a slight decrease in data fit. However, earthquake parameters, when we invert for them, and some structure imaged at the far edges of the model do account for a minor portion of the variance reduction. In this joint inversion we do not invert for station corrections given the inclusion of crustal structure and thickness in the tomographic model and topographic corrections already applied to the delay times.

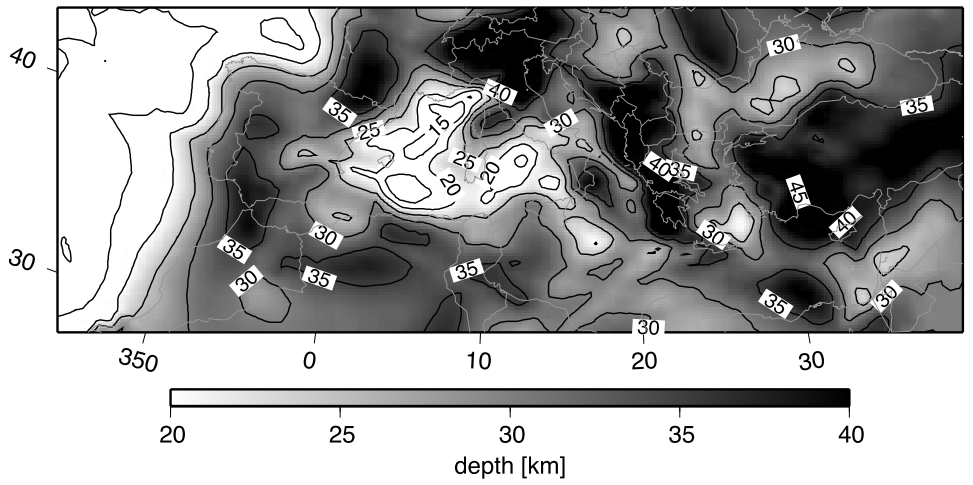

Figure 17. Map of Moho depth as determined from the joint inversion.

[44] The preferred joint model is shown for several depth sections in Figures 8c and 9b. In Figures 11–15 we show sections through the joint model with resolution tests. The updated map of Moho topography is shown in Figure 17. It is basically identical to the one of *Marone et al.* [2003], and the interpretations given there remain valid. Although the Moho map is mostly, but not everywhere, consistent with the assumption of isostasy, as demonstrated by *Marone et al.* [2003], it is superior to maps derived from isostasy considerations alone [*Jiménez-Munt et al.*, 2003] because it is constrained by more direct measurements of Moho depth.

6.4.1. Shallow Upper Mantle

[45] At shallow depths, the imaged structure is dominated by the regional waveform data. Consequently, many of our interpretations for the shallow mantle confirm those of *Marone et al.* [2004]. Beneath Europe, around 150 km, high velocities are imaged below the southern Alps, the Apennines, and southern Greece, including Crete and the Aegean Sea, related to subducted lithosphere still attached to lithosphere at the surface of the Adriatic and African Plates. The high-velocity lithosphere of the Adriatic Plate appears to dip southwestward beneath Italy, reaching progressively deeper from south to north along the Apennines. Beneath the northern Apennines the Adriatic lithosphere reaches a maximum depth of 250 km. Further north, just south of the western Alps, deeper high-velocity structures can be found but we deem it more plausible that these are related to subducted lithosphere form the Alpine Tethys Ocean. The high-velocity body between 150 and 300 km beneath the Tyrrhenian Sea is either interpreted as subducted lithosphere from the Ionian Sea or from the Adriatic Sea. If the latter, this piece has detached from the Adriatic lithosphere presently at the surface *Wortel and Spakman* [2000]. While it is tempting to interpret this piece as solely due to subduction of the Ionian Sea lithosphere, its geometry not aligning perfectly with the deep Wadati-Benioff zone suggests that part of this anomaly could be detached Adriatic lithosphere. In neither interpretation does the Adriatic lithosphere penetrate deep into the upper mantle. The inferred continuity of the Calabrian slab from the trench to the transition zone beneath Sardinia and the Algero-Provencal Basin is rather based on the Wadato-Benioff zone than on our tomographic model, which suggests no such continuity. A smaller high-velocity body is particularly strong between 200 and 300 km beneath the Vrancea region and coincides with the zone of intermediate-depth earthquakes there (Figure 14). The top 100 km of the Vrancea region show extremely low velocities.

[46] The remainder of the region is dominated by low velocities that are strongest and shallowest beneath south central and southeastern Europe, Turkey and the middle East, and Algeria. The eastern Atlantic Ocean shows high velocities down to about 90 km on average. A region of old ocean floor about 500 km in diameter and centered near the Josephie Seamount off southern Portugal, as well as the Bay of Biscay are underlain by a thicker high-velocity lithosphere, reaching slightly deeper than 100 km. The high-velocity lithosphere beneath the Azores and Mid-Atlantic Ridge appears to be significantly thinner and low asthenospheric velocities appear at shallower depths. At about 150 km the whole eastern Atlantic Ocean shows low asthenospheric velocities. This lithosphere-asthenosphere structure is typical for oceans [*Nishimura and Forsyth*, 1989] and matches well with cooling models. Structures more than 200 km below the Atlantic Ocean are not resolved because of the low level of higher mode excitation by the shallow and moderate-magnitude Mid-Atlantic Ridge earthquakes.

[47] Patches of Atlantic lithosphere style high-velocity structures have also been imaged in the western Mediterranean basins (Algero-Provencal basin, Tyrhennian Sea), the Ionian Sea, and the westernmost Black Sea. Beneath the Ionian and Black Sea the velocities are stronger an extend deeper than beneath the Atlantic while beneath the western Mediterranean they are not nearly as deep as beneath the Atlantic. An interpretation as oceanic lithosphere agrees with the relatively old and young age, respectively, of these ocean basins as well as with the detection of basalts from recent seafloor spreading in the Tyrrhenian Sea. The western Mediterranean is underlain by widespread low velocities, while the eastern Mediterranean has no such low-velocity layer. This difference might indicate that potentially extended African continental lithosphere could be underlying the eastern Mediterranean *Marone et al.* [2004]. The thickest lithosphere presently at the surface in the region is about 110 km thick beneath the Adriatic Sea.

6.4.2. Deep Upper Mantle

[48] The transition zone of the joint model is extensively populated with high-velocity anomalies. The joint models shows notably fast material beneath southernmost Spain, Calabria, the southern Alps and the Hellenic arc, including Cyprus. The fast features appear more consolidated in comparison with the model derived from regional waveform data and more complete in comparison with the model derived from traveltimes.

[49] The transition zone, between 410 and 660 km, shows a continuous belt of high velocities extending approximately linearly from southern Spain and the Alboran Sea to the eastern part of the Alps. Beneath the Alboran Sea the transition zone anomalies also are continued to shallower depths in a similar fashion as below the Alps (Figures 11 and 12). This most likely represents subducted lithosphere from the Alpine Tethys Ocean [*Stampfli and Borel*, 2004]. The NW-SE belt of high velocities in the eastern half of the region also represents subducted lithosphere no longer attached to present surface subduction, except in the south, where African Plate lithosphere continues to subduct beneath the Hellenic Arc, but not beneath Cyprus, according to our tomography.

[50] Our images of the *S* velocity heterogeneity at transition zone depths resemble those of *P* velocity anomalies (*Bijwaard et al.* [1998], *Piromallo and Morelli* [2003]). The correlation between *P* and *S* anomalies confirms that much of the observed velocity anomalies, in particular the high-velocity ones, are likely caused by thermal anomalies.

[51] An isolated, though likely smeared to the SW, low-velocity anomaly has been imaged in the transition zone beneath the Ionian Sea, east of Sicily. This anomaly is the only low-velocity feature that persists to depths as deep as the top of the lower mantle. Anomalies in this region are relatively unresolved in previous studies because of a lack of seismic data there. However, the expanded and unique new data coverage provided by the MIDSEA stations [*van der Lee et al.*, 2001b] helped us resolve structure beneath

the southern Mediterranean Sea. Coincidentally, *Montelli et al.* [2004a, 2004b] imaged low *P* velocities deep beneath the Ionian Sea by using finite frequency sensitivity kernels when inverting *P* delays.

6.4.3. Lower Mantle Down to 1400 km

[52] Below the upper mantle our joint model still shows a considerable distribution of high-velocity anomalies, though concentrated in the eastern part of the region, where considerably more oceanic lithosphere existed throughout the geologic past than in the western part [*Dercourt et al.*, 1986; *Stampfli and Borel*, 2004] Most of these deep high-velocity anomalies have no direct connection with lithosphere presently at the surface, except for the north dipping Hellenic slab beneath Greece. The Hellenic slab appears fairly continuous all the way from the Hellenic trench south of Crete down into the lower mantle to about 1200 km, consistent with the earliest images of this phenomenon [*Spakman et al.*, 1993]. The Hellenic slab (Figure 14) seems to flatten slightly before it continues with a more vertical dip in the lower mantle. The slab's dip is more than suggested by regional waveform inversions alone but less than suggested by arrival time data alone. The high-velocity anomaly of the Hellenic slab is stronger at 600 and 1000 km than at 800 km. This phenomenon was originally thought to be an artifact [*Spakman et al.*, 1993] but persists in our better resolved model and could reflect a mode of lower mantle penetration that is rather discrete than continuous in time.

[53] In the case of the Calabrian subduction, the clear presence of a Wadati-Benioff earthquake zone (Figure 13) indicates the presence of a continuous slab down to 500 km, but such a feature is only barely imaged in our model (Figure 13). Ionian lithosphere subducting beneath the Calabrian arc significantly flattens in the transition zone and has no corresponding lower mantle component (Figure 13). If the high-velocity anomaly in the transition zone beneath Sardinia and the Algero-Provencal Basin represents Ionian lithosphere, its relatively flat geometry and absence of high-velocity material in the lower mantle suggests that the lithosphere is too buoyant to penetrate into the lower mantle.

[54] The high-velocity anomaly 1000–1200 km beneath the Ionian Sea most likely represents subducted lithosphere from the Vardar Ocean [*Stampfli and Borel*, 2004]. The high-velocity anomaly deeper than 1200 km beneath Turkey and the Black Sea most likely represents subducted lithosphere from the Neo-Tethys, as previously suggested by *Van der Voo et al.* [1999].

7. Conclusions

[55] We have presented a new *S* wave velocity model for the Africa-Eurasia plate boundary region. The resolution for this model is higher than previous *S* velocity models inferred from body wave arrival times because we have enhanced standard arrival time data sets with our own measurements of relative arrival times at stations of the MIDSEA and other broadband stations in the region. Our *S* velocity model is superior to EAV03, which is inferred from regional waveforms, because our model also explains arrival times of teleseismic body waves and it covers a larger volume of the mantle than regional waveform inversions alone, with fair resolving power down to 1400 km. We find that the teleseismic arrival times and regional waveforms are compatible data sets and predominantly sense, in different ways, the same mantle structures. We have shown models exist that fit both data nearly as well as when inverting the data individually.

[56] Our model shows high-velocity lithosphere at shallow depths underlain by low-velocity asthenosphere in the Atlantic Ocean, Ionian Sea, and the western Mediterranean basins, confirming their oceanic nature. For the older oceanic structures, the Ionian Sea and the eastern Atlantic Ocean, we image a thicker lithosphere than for the younger basins, the Algero-Provencal basin and the Tyrrhenian Sea. The structure imaged beneath the eastern Mediterranean basin does not resemble this typical oceanic lithosphere over asthenosphere structure. However, its low elevation and attachment to the long high-velocity most likely ocean lithosphere of the Hellenic slab suggests that the eastern Mediterranean basin rather represents a continental shelf than a typical continental structure. Thus the eastern Mediterranean region might represent a natural laboratory for the beginning of a continental collision.

[57] Between about 120 and 300 km the region, including its continental parts, is dominated by low velocities interspersed with high-velocity anomalies associated with subduction of the African Plate at the Hellenic trench, Ionian Sea lithosphere at the Calabrian trench, and Adriatic lithosphere beneath Italy. The Adriatic slab does not extend deeper than 250 km and its southern portion appears detached from the northern portion and from the Adriatic lithosphere at the surface. Our model shows that slab penetration into the lower mantle occurs only for the Hellenic subduction zone in the eastern part of our study region. The subducting lithosphere represents the westernmost pats of the Neo-Tethys Ocean, perhaps including the Lycian and/or Pindos seas [*Stampfli and Borel*, 2004] and persists with a strong high-velocity signature northward and downward to about 1200 km. Indeed, the fact that lower mantle penetration occurs shows that a relatively large plate is/was subducting for a longer period of time, thus enabling it to penetrate the 660 km.

[58] This is not the case for the smaller Alpine Tethys Ocean that subducted in the central and western Mediterranean. This Ocean was of a relative young age and thus might have lacked the persistence to subduct to lower mantle depths and instead became deflected at the 660 km discontinuity. However, the transition zone bears signatures of most of these oceans and is thus dominated by high-velocity anomalies. The only low-velocity anomaly in the transition zone lies beneath the Ionian Sea and is underlain by the lower mantle high-velocity anomaly that we interpret as lithosphere of the subducted Vardar Ocean. Whether or not this low-velocity anomaly is associated with Etna volcanism, as suggested by *Montelli et al.* [2004b] cannot be resolved with our tomographic model. Geochemical data [*Tanguy et al.*, 1997; *Schiano et al.*, 2001] indeed require a deeper plume type source for the Etna.

[59] **Acknowledgments.** CS and the MIDSEA data acquisition effort were supported by the Swiss NF. S.v.d.L. acknowledges support from the U.S. DOE under contract DE-FC52-04NA25541. We also thank the Carnegie Institution of Washington for supporting the initial development of the new, joint inversion method applied here. This work would not have been accomplished without the data acquisition efforts of the MIDSEA participants, spearheaded by Federica Marone, Mark van der Meijde, Anne

Deschamps, Lucia Margheriti, Peter Burkett, Sean Soloman, Paulo Alves, Makis Chouliaras, Abdurazzag Eshwehdi, Marijan Herak, Ramon Ortiz, Jose Martin Davila, Arantza Ugalde, Josep Vila, and Karim Yelles. We thank Michael West and an anonymous reviewer for constructive comments that led to major improvements in the presentation of our work.

References

Baer, M. (1990), The seismic network of the Swiss Seismological Service, in *Workshop on MedNet, the Broad-Band Seismic Network for the Mediterranean*, edited by E. Boschi, D. Giardini, and A. Morelli, pp. 345–350, Ist. Naz. Geofis., Rome.

Bijwaard, H. (1999), Seismic travel-time tomography for detailed global mantle structure, Ph.D. thesis, Univ. of Utrecht, Utrecht, Netherlands.

Bijwaard, H., W. Spakman, and E. R. Engdahl (1998), Closing the gap between regional and global travel time tomography, *J. Geophys. Res.*, *103*, 30,055–30,078.

Boschi, E., D. Giardini, and A. Morelli (1991), MedNet: the very broadband seismic network for the Mediterranean, *Nuovo Cimento*, *14*, 79–99.

Buforn, E., M. Bezzeghoud, A. Udías, and C. Pro (2004), Seismic sources on the Iberian-African Plate boundary and their tectonic implications, *Pure Appl. Geophys.*, *161*, 623–646.

Calvert, A., E. Sandvol, D. Seber, M. Barazangi, S. Roecker, T. Mourabit, F. Vidal, G. Alguacil, and N. Jabour (2000), Geodynamic evolution of the lithosphere and upper mantle beneath the Alboran region of the western Mediterranean: Constraints from travel time tomography, *J. Geophys. Res.*, *105*, 10,871–10,898.

Constable, S. C., R. L. Parker, and C. G. Constable (1987), Occam's inversion: A practical algorithm for generating smooth models from electromagnetic sounding data, *Geophysics*, *52*, 289–300.

Das, T., and G. Nolet (1995), Crustal thickness estimation using high-frequency Rayleigh-waves, *Geophys. Res. Lett.*, *22*, 539–542.

Das, T., and G. Nolet (1998), Crustal thickness map of the western United States by portitioned waveform inversion, *J. Geophys. Res.*, *103*, 30,021–30,038.

Dercourt, J., et al. (1986), Geological evolution of the Tethys Belt from the Atlantic to the Pamirs since the Lias, *Tectonophysics*, *123*, 241–315.

Dewey, J., M. Helman, E. Turco, D. Hutton, and S. Knott (1989), Kinematics of the western Mediterranean, in *Alpine Tectonics*, edited by M. Coward, D. Dietrich, and R. Park, *Geol. Soc. Spec. Publ.*, *45*, 265–283.

Diehl, T. (2003), Die Krustenstruktur Südost-Rumäniens aus der Analyse teleseismischer Receiver Funktionen, Master's thesis, Univ. Karlsruhe, Karlsruhe, Germany.

Dziewonski, A. M., A. L. Hales, and E. R. Lapwood (1975), Parametrically simple Earth models consistent with geophysical data, *Phys. Earth. Planet. Inter.*, *10*, 12–48.

Engdahl, E. R., R. van der Hilst, and R. Buland (1998), Global teleseismic earthquake relocation with improved travel times and procedures for depth determination, *Bull. Seismol. Soc. Am.*, *88*, 722–743.

Hanka, W., and R. Kind (1994), The GEOFON program, *IRIS Newslett*, *13*, 1–4.

Huber, P. J. (1981), *Robust Statistics*, John Wiley, New York.

Jiménez-Munt, I., R. Sabadini, A. Gardi, and G. Bianco (2003), Active deformation in the Mediterranean from Gibraltar to Anatolia inferred from numerical modeling and geodetic and seismological data, *J. Geophys. Res.*, *108*(B1), 2006, doi:10.1029/2001JB001544.

Jolivet, L., and C. Faccenna (2000), Mediterranean extension and the Africa-Eurasia collision, *Tectonics*, *19*, 1095–1106.

Kennett, B. L. N., and E. R. Engdahl (1991), Traveltimes for global earthquake location and phase identification, *Geophys. J. Int.*, *105*, 429–465.

Lippitsch, R., E. Kissling, and J. Ansorge (2003), Upper mantle structure beneath the Alpine orogen from high-resolution teleseismic tomography, *J. Geophys. Res.*, *108*(B8), 2376, doi:10.1029/2002JB002016.

Marone, F., M. van der Meijde, S. van der Lee, and D. Giardini (2003), Joint inversion of local, regional and teleseismic data for crustal thickness in the Eurasia-Africa plate boundary region, *Geophys. J. Int.*, *154*, 499–514.

Marone, F., S. van der Lee, and D. Giardini (2004), Three-dimensional upper-mantle *S*-velocity model for the Eurasia-Africa plate boundary region, *Geophys. J. Int.*, *158*, 109–130.

Montelli, R., G. Nolet, F. A. Dahlen, G. Masters, E. R. Engdahl, and S. H. Hung (2004a), Finite-frequency tomography reveals a variety of plumes in the mantle, *Science*, *303*, 338–343.

Montelli, R., G. Nolet, G. Masters, F. A. Dahlen, and S. H. Hung (2004b), Global *P* and *PP* traveltime tomography: Rays versus waves, *Geophys. J. Int.*, *158*, 637–654.

Nishimura, C. E., and D. W. Forsyth (1989), The anisotropic structure of the upper mantle in the Pacific, *Geophys. J. R. Astron. Soc.*, *96*, 203–229.

Nolet, G. (1990), Partitioned waveform inversion and two-dimensional structure under the network of autonomously recording seismographs, *J. Geophys. Res.*, *95*, 8499–8512.

Panza, G., S. Mueller, and G. Calcagnile (1980), The gross features of the lithosphere-asthenosphere system in Europe from seismic surface waves and body waves, *Pure Appl. Geophys.*, *118*, 1209–1213.

Pasyanos, M., and W. Walter (2002), Crust and upper mantle structure of North Africa, Europe, and the Middle East from inversion of surface waves, *Geophys. J. Int.*, *149*, 464–482.

Piromallo, C., and A. Morelli (2003), *P* wave tomography of the mantle under the Alpine-Mediterranean area, *J. Geophys. Res.*, *108*(B2), 2065, doi:10.1029/2002JB001757.

Ritsema, J., H.-J. van Heijst, and J. H. Woodhouse (1999), Complex shear wave velocity structure imaged beneath Africa and Iceland, *Science*, *286*, 1925–1928.

Röhm, A. H. E., H. Bijwaard, W. Spakman, and J. Trampert (2000), Effects of arrival time errors on traveltime tomography, *Geophys. J. Int.*, *142*, 270–276.

Romanowicz, B., M. Cara, J. F. Fels, and D. Rouland (1984), Geoscope; A French initiative in long-period three-component global seismic networks, *Eos Trans. AGU*, *65*(42), 753.

Scales, J. A. (1987), Tomographic inversion via the conjugate gradient method, *Geophysics*, *52*, 179–185.

Schiano, P., R. Clocchiatti, L. Ottolini, and T. Busà (2001), Transition of Mount Etna lavas from a mantle-plume to an island-arc magmatic source, *Nature*, *412*, 900–904.

Schmid, C., S. van der Lee, and D. Giardini (2004), Delay times and shear wave splitting in the Mediterranean region, *Geophys. J. Int.*, *159*, 275–290.

Selvaggi, G., and C. Chiarabba (1995), Seismicity and *P*-wave velocity image of the Southern Tyrrhenian subduction zone, *Geophys. J. Int.*, *122*, 818–826.

Spakman, W., S. van der Lee, and R. D. van der Hilst (1993), Travel-time tomography of the European-Mediterranean mantle down to 1400 km, *Phys. Earth Planet. Inter.*, *79*, 3–74.

Stampfli, G. M., and G. D. Borel (2004), The TRANSMED Transects in space and time: Constraints on the Paleotectonic evolution of the Mediterranean Domain, in *The TRANSMED Atlas*, edited by W. E. Cavazz, pp. 53–80, Springer, Berlin.

Tanguy, J.-C., M. Condomines, and G. Kieffer (1997), Evolution of the Mount Etna magma: Constraints on the present feeding system and eruptive mechanism, *J. Volcanol. Geotherm. Res.*, *75*, 221–250.

van der Lee, S. (1990), Tomographic inversion of delay times for *P*-velocities beneath Europe, Master's thesis, Univ. of Utrecht, Utrecht, Netherlands.

van der Lee, S., and G. Nolet (1997), Upper mantle *S* velocity structure of North America, *J. Geophys. Res.*, *102*, 22,815–22,838.

van der Lee, S., D. James, and P. Silver (2001a), Upper mantle *S* velocity structure of western and central South America, *J. Geophys. Res.*, *106*, 30,821–30,834.

van der Lee, S., et al. (2001b), Eurasia-Africa plate boundary region yields new seismographic data, *Eos Trans. AGU*, *82*(51), 637.

VanDecar, J. C. (1991), Upper-mantle structure of the Cascadia subduction zone from non-linear teleseismic travel-time inversion, Ph.D. thesis, Univ. of Wash., Seattle.

VanDecar, J. C., and R. S. Crosson (1990), Determination of teleseismic relative phase arrival times using multi-channel cross-correlation and least-squares, *Bull. Seismol. Soc. Am.*, *80*, 150–169.

Van der Voo, R., W. Spakman, and H. Bijwaard (1999), Tethyan subducted slabs under India, *Earth Planet. Sci. Lett.*, *171*, 7–20.

Wang, Z., and F. A. Dahlen (1995), Spherical-spline parametrization of three-dimensional Earth models, *Geophys. Res. Lett.*, *22*, 3099–3102.

West, M., W. Gao, and S. Grand (2004), A simple approach to the joint inversion of seismic body and surface waves applied to the southwest U.S., *Geophys. Res. Lett.*, *31*, L15615, doi:10.1029/2004GL020373.

Wortel, M. J. R., and W. Spakman (2000), Subduction and slab detachment in the Mediterranean-Carpathian region, *Science*, *290*, 1910–1917.

Zielhuis, A. (1992), *S*-wave velocity below Europe from delay-time and waveform inversions, Ph.D. thesis, Univ. of Utrecht, Utrecht, Netherlands.

Zielhuis, A., and G. Nolet (1994), Shear-wave velocity variations in the upper mantle beneath central Europe, *Geophys. J. Int.*, *117*, 695–715.

E. R. Engdahl, Department of Physics, University of Colorado, Campus Box 390 UCB, Boulder, CO 80309-0390, USA. (engdahl@colorado.edu)

D. Giardini, Institute of Geophysics, Schafmattstr. 30, ETH Zurich HPP P 6.1, CH-8093 Zürich, Switzerland. (giardini@seismo.ig.erdw. ethz.ch)

C. Schmid, Schweizerische Mobiliar Versicherungsgesellschaft, Bundesgasse 35, Postfach, CH-3001 Bern, Switzerland. (christian.schmid1@mobi.ch)

J. C. VanDecar, Department of Terrestrial Magnetism, Carnegie Institute of Washington, Washington, DC 20015-1305, USA. (vandecar@dtm.ciw.edu)

S. van der Lee, Department of Earth and Planetary Sciences, Northwestern University, 1850 Campus Drive, Evanston, IL 60208, USA. (suzan@earth.northwestern.edu)